

Density and Shape Effects in the Acoustic Propulsion of Bimetallic Nanorod Motors

Suzanne Ahmed,[†] Wei Wang,[‡] Lanjun Bai,[‡] Dillon T. Gentekos,[†] Mauricio Hoyos,[§] and Thomas E. Mallouk^{*,†}

[†]Departments of Chemistry, Physics, and Biochemistry and Molecular Biology, The Pennsylvania State University, University Park, Pennsylvania 16802, United States

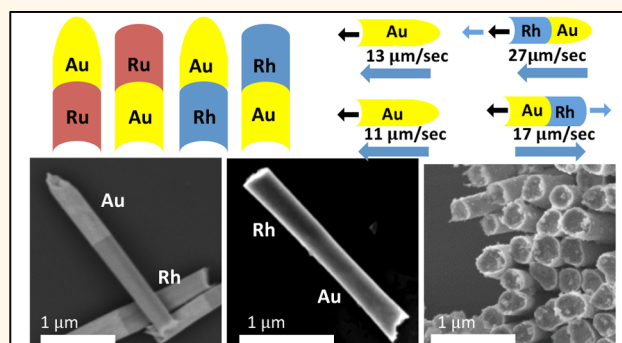
[‡]School of Materials Science and Engineering, Shenzhen Graduate School, Harbin Institute of Technology, Shenzhen 518055, China

[§]Laboratoire de Physique et Mécanique des Milieux Hétérogènes, UMR7636 CNRS, UMPC, ESPCI, 10 rue Vauquelin, 75005 Paris, France

S Supporting Information

ABSTRACT: Bimetallic nanorods are propelled without chemical fuels in megahertz (MHz) acoustic fields, and exhibit similar behaviors to single-metal rods, including autonomous axial propulsion and organization into spinning chains. Shape asymmetry determines the direction of axial movement of bimetallic rods when there is a small difference in density between the two metals. Movement toward the concave end of these rods is inconsistent with a scattering mechanism that we proposed earlier for acoustic propulsion, but is consistent with an acoustic streaming model developed more recently by Nadal and Lauga (*Phys. Fluids* 2014, 26, 082001). Longer rods were slower at constant power, and their speed was proportional to the square of the power density, in agreement with the acoustic streaming model. The streaming model was further supported by a correlation between the disassembly of spinning chains of rods and a sharp decrease in the axial speed of autonomously moving motors within the levitation plane of the cylindrical acoustic cell. However, with bimetallic rods containing metals of different densities, a consistent polarity of motion was observed with the lighter metal end leading. Speed comparisons between single-metal rods of different densities showed that those of lower density are propelled faster. So far, these density effects are not explained in the streaming model. The directionality of bimetallic rods in acoustic fields is intriguing and offers some new possibilities for designing motors in which shape, material, and chemical asymmetry might be combined for enhanced functionality.

KEYWORDS: nanomotor, acoustic motor, ultrasonic propulsion, bimetallic nanomotors



Artificial nano- and microswimmers are of growing interest because they provide insight into the emergent and collective behavior of motile living systems, as well as new functionality and applications in biomedicine, analysis, separations, environmental chemistry, and materials science.^{1–10} The recent discovery that rocket-shaped metallic nanorods can be propelled in fluids by acoustic energy in the megahertz (MHz) regime presents some promise for use in biomedical applications.¹¹ Recent reports of acoustic nanomotors have demonstrated their fuel-free propulsion and steering in buffer solutions, their actuation within living cells, and as their use in biochemical analysis and drug delivery.^{12–17} Their collective behavior and assembly have also been explored.^{18–20}

To design acoustic motors that can carry out useful functions, it is important to understand the mechanism of their propulsion as well as the factors that affect their speed and

directionality. In a typical experiment, the nanorods are confined to a levitation plane by acoustic energy that is generated at the base of the cell, as illustrated in Figure 1. Experimental and more recently theoretical research have suggested mechanisms in which the shape asymmetry of the rods results in motion within the levitation plane, *i.e.*, perpendicular to the direction of acoustic excitation.^{11,21,22} A recent paper by Nadal and Lauga proposed that the movement arises from an acoustic streaming effect.²² In their model, the oscillation of the nanorod in the direction of the acoustic excitation (the vertical direction in Figure 1) generates a streaming flow. That flow in turn exerts stresses on the asymmetric particle that drive its oscillation in the levitation

Received: February 23, 2016

Accepted: March 18, 2016

Published: March 18, 2016

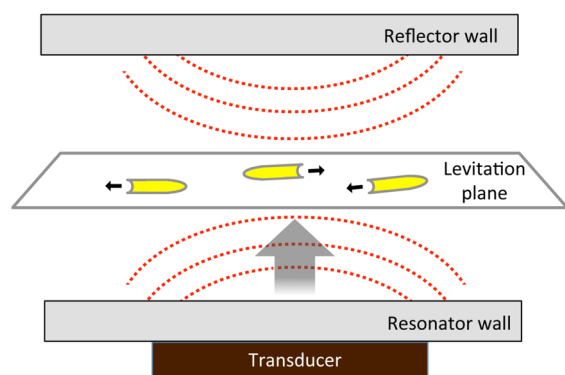


Figure 1. Schematic illustration of the autonomous movement of axisymmetric gold nanorods (not drawn to scale) in an acoustic cell. Acoustic waves are launched by the transducer at the bottom of the cell. At the resonant frequency, a standing wave is created that levitates the rods to the midplane of the cell where they undergo rapid in-plane movement.

plane. Because the density of the nanorods is higher than that of the surrounding fluid, their inertia is significant at high driving frequency. Consequently, if the particle is asymmetric, the streaming effect results in a net force along the axis of the rod, propelling it toward its concave end.

In the acoustic streaming model, the nanorods are treated as rigid bodies, and thus it is not obvious how any asymmetry in their composition or density might affect their propulsion. Here, we explore experimentally the additional effect of material asymmetry of nanorod motors, and also measure the effects of rod length and acoustic power. We find that bimetallic rods exhibit a consistent and predictable polarity in their axial motion, with the lighter end always leading. Both the length- and power-dependence of nanorod speed are consistent with acoustic streaming as the dominant mechanism of propulsion. However, the density dependence of the direction of motion suggests that additional elaboration of the theory is needed.

RESULTS AND DISCUSSION

Fabrication of Asymmetric Nanorods. Single metal and bimetallic nanorods containing Au, Rh, Pd, Ag, Pt and Ru segments were fabricated by electrochemical deposition within the pores of anodic alumina membranes. A sacrificial silver segment was first plated into the pores, and the appropriate metals were then sequentially plated. Because the sacrificial silver segment typically has a convex tip, the first metal plated on it forms the concave end of the asymmetric nanorod. Depending on the surface interaction between the second metal and the alumina pore walls, the second metal segment can have a flat tip, or a convex tip, as shown in Figure 2.

Powered Movement of Nanorods in the Levitation Plane. Acoustic excitation of nanorod motors was carried out in a cylindrical acoustic chamber (with a height of 180 μm and diameter of 5 mm) operated at a resonant frequency of *ca.* 4 MHz as previously described.¹¹ At resonance, a bulk acoustic standing wave is set up and the rods are levitated to the midpoint plane of the chamber. In this plane, rods undergo random autonomous motion as well as aggregation within lateral nodes, and polar spinning chains of rods also form.¹¹ The spatial distribution of these different modes of propulsion can be seen in Figure 3 and Video S1 (see Supporting Information). Random autonomous motion tends to occur far from the nodal aggregates and spinning chains, as shown in

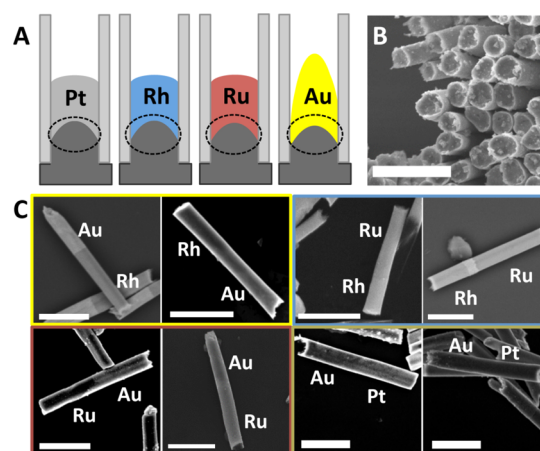


Figure 2. (A) Schematic drawing of the shapes of bimetallic nanorods. The segment deposited first replicates the convex silver segment (black dashed circle) and is therefore concave. At the other end, Rh, Ru, and Pt acquire a flat shape, while Au is typically convex. (B) Field emission scanning electron microscope (FE-SEM) images of the concave (deposited first) nanorod ends after dissolution of the sacrificial silver segment and release from the membrane. Scale bar is 1 μm . (C) FE-SEM images of bimetallic rods. Top row (metals listed in the order deposited): AuRh ($2.3 \pm 0.3 \mu\text{m}$; Au, $1.3 \pm 0.2 \mu\text{m}$; Rh, $1.0 \pm 0.2 \mu\text{m}$); RhAu ($2.1 \pm 0.4 \mu\text{m}$; Rh, $1.04 \pm 0.3 \mu\text{m}$; Au, $1.04 \pm 0.1 \mu\text{m}$); RuRh ($1.6 \pm 0.2 \mu\text{m}$; Ru, $1.3 \pm 0.1 \mu\text{m}$; Rh, $0.5 \pm 0.1 \mu\text{m}$); RhRu ($2.6 \mu\text{m}$; Rh, 0.9; Ru, $1.6 \mu\text{m}$). A short Au segment was grown within the RhRu rod to allow for controlled Ru growth on top of Rh. In the absence of the Au segment, the Ru segment, deposited at a constant potential, overgrew within seconds on the catalytic Rh metal. Bottom row (metals listed in the order deposited): RhAu ($2.2 \pm 0.3 \mu\text{m}$; Au, $1.0 \pm 0.2 \mu\text{m}$; Ru, $1.0 \pm 0.1 \mu\text{m}$); AuRh ($2.3 \pm 0.3 \mu\text{m}$; Ru, 1.2 ± 0.3 ; Au, 1.1 ± 0.2); AuPt ($2.2 \pm 0.2 \mu\text{m}$; Au, $1.2 \pm 0.2 \mu\text{m}$; Pt, $1.0 \pm 0.2 \mu\text{m}$); PtAu ($2.0 \pm 0.1 \mu\text{m}$; Pt, $1.0 \pm 0.1 \mu\text{m}$; Au, $0.9 \pm 0.08 \mu\text{m}$). All scale bars are 1 μm .

Figure 3A. Between the region of autonomous motion and the nodal aggregate, the rods travel in orbits within the levitation plane. As the distance from the nodal aggregates increases, these orbits become larger (Figure 3D). At distances greater than about 500 μm from the nodes, the orbits become very large and there is no apparent curvature to their axially directed motion (Video S2).

The appearance of orbits of increasing radius can be understood as the combination of the two primary forces in the levitation plane: the lateral component of the acoustic radiation force and the streaming-induced drag force along the axis of the rod. The radiation force serves to push the rods toward the nodes, whereas the streaming force propels the rods along their axis.²⁴ The combination of both forces results in orbital motion. With increasing distance from the nodes, the radiation force becomes weaker, and the orbital radius increases, until eventually only axial movement is observed.

The magnitudes of the different forces on nanorods in the cylindrical acoustic cell used in these experiments have previously been estimated.¹¹ The acoustic radiation force in the vertical direction (*ca.* 0.75 pN) is responsible for levitation. The axial propulsion force for a rod 2 μm long, 300 nm diameter rod moving at 200 $\mu\text{m}/\text{s}$ is comparable to the vertical radiation force, *ca.* 1 pN. In contrast, the acoustic radiation force in the lateral direction is smaller and decreases with increasing distance from the lateral nodes.

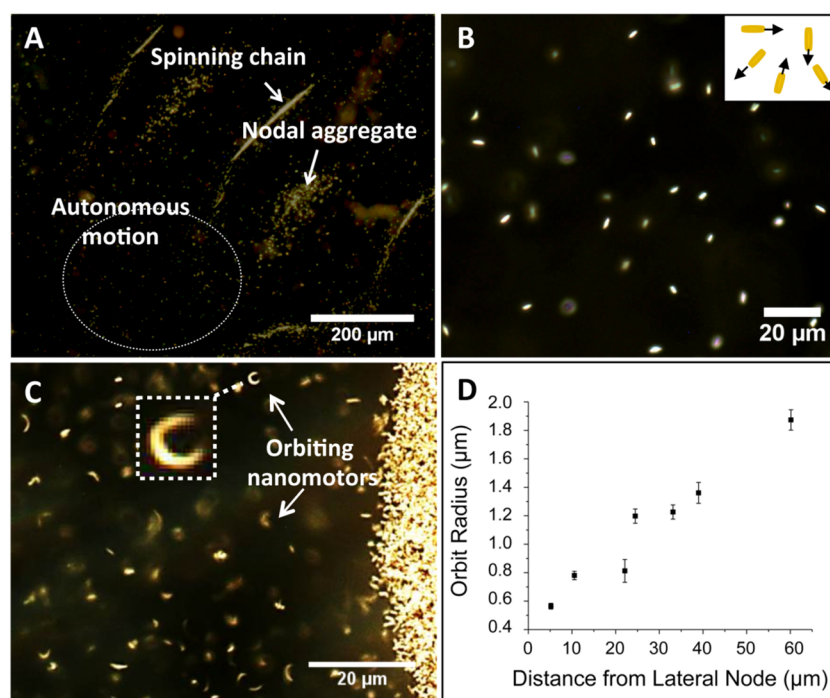


Figure 3. Spatial distribution of nanorod movement in the cylindrical acoustic cell. (A) Low magnification optical micrograph showing the distribution of spinning chains, nodal aggregates and autonomous motion. (B) Zoomed in optical micrograph and a schematic of autonomous motion in random directions. (C) Orbital motion of rods at the periphery of a nodal aggregate. Snapshots of orbiting motion were taken at a low frame rate (30 s^{-1}), resulting in blurring of the images of orbiting rods. See [Video S2](#). (D) Radius of orbits vs distance from nodes.

Directionality of Bimetallic Rods. To study the shape- and density-dependence of rod speeds in the regions of autonomous motion, bimetallic rods were fabricated in the combinations listed in [Table 1](#). These particular combinations

Table 1. Bimetallic Nanorods Studied and the Leading End in Autonomous Axial Motion^a

bimetallic rod	lower density end	leading end
AuRu	Ru	Ru
RuAu	Ru	Ru
AuRh	Rh	Rh
RhAu	Rh	Rh
AuPt	Au	Au
PtAu	Au	Pt
AuPd	Pd	Pd
AuAg	Ag	Ag
RuRh	Ru	Ru

^aThe metal segments are listed in the order plated; hence, the end of the first metal listed is always concave.

were selected because the two segments were distinguishable by color in the optical microscope, and hence, the direction of movement could be determined.²⁵ The densities of the pure metals are listed in [Table S1](#).

The data in [Table 1](#) show a clear relationship between the direction of motion and the composition of bimetallic rods, *i.e.*, that the lighter end is typically the leading end. However, the rods are also asymmetric in shape, because the end plated first is concave, and we know from earlier studies that shape asymmetry is also important in determining the direction of motion. To deconvolute the effects of material and shape asymmetry, the order of electrodeposition was reversed for AuRu, AuRh, RuRh, and AuPt rods, yielding RuAu, RhAu,

RhRu, and PtAu, respectively. When the two metal segments had similar densities (AuPt, or combinations of lighter metals), the motion of the rod was always toward the concave end. In contrast, in cases where the bimetallic rod contained a heavy Au or Pt segment and a segment of less dense metal (Ru, Rh, Pd, Ag, or Ru), the motion was always toward the lighter end, regardless of which end was concave. Taken together, these data show that the direction of motion of bimetallic rods is determined predominantly by material asymmetry.

Movement toward the concave end, which was observed with AuPt and PtAu, is predicted by calculations on axisymmetric near-spheres that have opposing convex and concave sides.¹⁶ We note that our own earlier model of pressure differences generated by scattering of acoustic energy from the convex and concave ends made the opposite prediction,⁵ and is thus inconsistent with the data. Indeed, for RuRh rods where the densities of the two metals are similar, the concave Ru end leads as well. For RhRu rods, a short Au segment was grown within the rod to allow for controlled Ru growth on top of Rh. As the Au segment was off-center, as can be seen in [Figure 1C](#), the opposite lower density end, Ru, was the leading end. To test further the effect of the presence of a third segment within a rod on the polarity of its motion, two sets of all-Au rods with an off-center Ru segment were fabricated, with Ru placed closer to the concave or convex end. In both cases, the half of the rod containing the lower density ruthenium segment was the leading end ([Figure S2](#)).

The effect of metal density on axial propulsion speed was evaluated more quantitatively by using mixtures of single-element, bimetallic, and Au rods. Lighter rods were consistently faster than heavier ones when observed in the same region of the cell. For example, the speed of Rh rods was approximately twice that of Au rods of the same length. Rods for which shape and material asymmetry reinforced each other (RhAu and

RuAu) were ~30% faster than those (AuRh and AuRu) for which the forces were opposed. The speeds of RhAu and RuAu were roughly twice those of Au rods. The trend from these experiments is that the effects of shape and material asymmetry are roughly additive. These results are summarized in Figure 4.

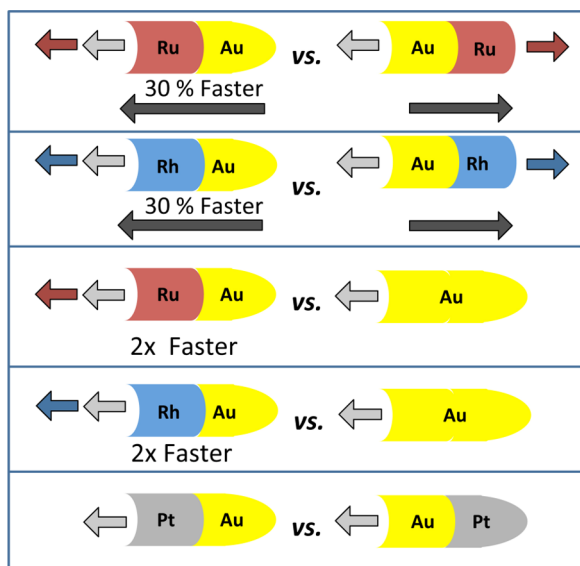


Figure 4. Relative speeds and directions of mono- and bimetallic rods propelled by ultrasound. The relative speeds of rods in mixtures were measured at constant frequency (3.77 MHz) and amplitude (10 Vpp) at the same location in the chamber. Light gray and colored arrows indicate the direction of forces arising from asymmetry in shape (always toward the concave end) and density (always toward the lighter end), respectively. Dark arrows show the observed direction of motion for cases in which shape and density effects can oppose each other.

In addition to density, two additional relevant material properties are the acoustic contrast factor and the specific acoustic impedance. The acoustic contrast factor Φ , which is proportional to the acoustic radiation force on a particle, is related to the densities of the particle and of the medium according to eq 1:^{26,27}

$$\Phi = \frac{5\rho_p - 2\rho_m}{2\rho_p + \rho_m} - \frac{\beta_p}{\beta_m} \quad (1)$$

Here ρ_p is the density of the metal particle and ρ_m is the density of the medium, in this case water. β_p and β_m are the compressibilities of the particle and medium, respectively, where

$$\beta_p = \frac{1}{\rho_p c_p^2} \quad (2)$$

and c_p is the speed of sound in the particle. The acoustic contrast factors for Au, Pt, Ru, Rh, Pd, and Ag were calculated to be 2.38, 2.39, 2.32, 2.32, 2.31, and 2.28, respectively. As the acoustic contrast factor is largely invariant for the metals in question in water, it cannot account for the large variation in speeds that we observe with different metals and bimetallic combinations.

The specific acoustic impedance of a metal is the product of its density and the speed of sound in the metal. Tabulated values of these quantities were used to calculate specific

acoustic impedances,^{28–30} which are listed in Table S2. Again, there is no apparent correlation between the observed direction of motion and these calculated values. It should be noted that the speed of sound in a metal can vary somewhat with the method by which it is fabricated, which affects grain size and porosity. However, these effects are unlikely to result in the strong correlation we observe between particle speed, direction, and metal density.

Length Dependence of Axial Speeds. Two predominant forces are exerted on particles suspended in fluids in an acoustic field. They are the primary acoustic radiation force and the acoustic streaming-induced drag force. Typically, the primary radiation force is dominant with particles that are micrometers in size or larger, whereas the motion of smaller particles is dominated by the streaming-induced drag force.^{24,31,32} Most research in this field has focused on spherical dielectric (e.g., polystyrene or silica) particles, and thus, the applicability of these critical diameters to cylindrical metal rods with concave and convex ends is unknown. Additionally, the dominance of one force over the other can depend on the cell design.²⁴

To determine which force(s) dominate the motion of metallic nanorods, the length dependence of their axial speed was measured. A mixture of Au nanorods in water was prepared using 1.3 μm long Au rods as an internal standard, and care was taken to monitor their movement at the same location within the acoustic chamber, in regions where the predominant mode of motion was autonomous propulsion along their axis (Video S4). The resulting experimental data were evaluated in terms of equations describing the length-dependent streaming-induced force.

Equation 3 describes the drag force on a cylindrical particle (approximated as a prolate ellipsoid) of length L and radius R moving at velocity v , and conversely eq 4 expresses the velocity as a function of the drag force and length L .

$$F_{\text{drag}} = \frac{2\pi\eta L}{\ln\left(\frac{L}{R}\right) - 0.72} v \quad (3)$$

$$v = F_{\text{drag}} \frac{\ln\left(\frac{L}{R}\right) - 0.72}{2\pi\eta L} \quad (4)$$

The acoustic power density at a particular frequency and amplitude should be roughly constant over the small observation volumes we used to compare the speeds of rod mixtures. A detailed theoretical treatment of an axisymmetric near-sphere shows that the streaming-induced drag force is proportional to the level of shape asymmetry of the particle.²² Here, the levels of shape asymmetry of the particles are similar as they are all made of gold and have the same diameter. Hence, we expect the propulsion force to vary only weakly with L . Since the velocity at a given force scales roughly as $1/L$ according to eq 4, a longer rod would move at a slower speed than a shorter one if the motion is driven by streaming-induced drag. This is indeed what is observed. In Figure 5, the relative axial velocity of the rods is plotted as a function of the coefficient of the drag force, as expressed in eq 4. The constant slope of the fit line indicates that the force is independent of length.

In contrast, we would expect the primary acoustic radiation force to increase with rod length. For example, for spherical particles the radiation force is proportional to the particle volume,²⁷ and because the drag coefficient is proportional to

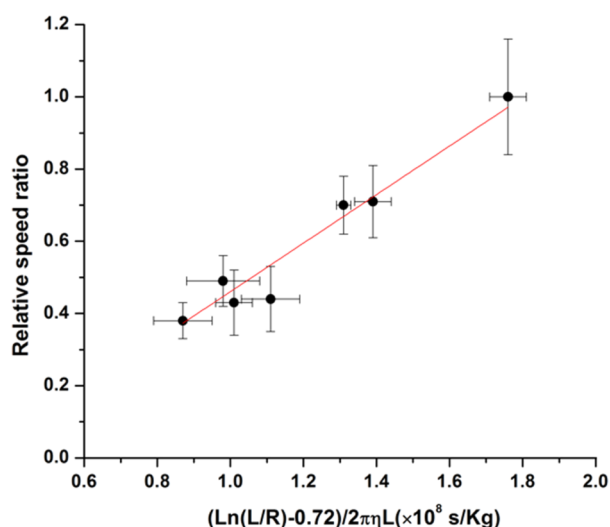


Figure 5. Relative speeds of 300 nm diameter gold nanorods of different lengths as a function of the coefficient of the drag force in eq 4.

the sphere radius, larger spheres are propelled faster by the radiation force. The opposite trend that we observe (longer rods move slower) and the fact that the autonomous motion is not directed toward the lateral nodes in the cell confirm that the primary radiation force is weak relative to the streaming-induced drag force in the axial propulsion of the nanorods. These observations are consistent with the model of Nadal and Lauga.²²

Power Dependence of Streaming-Induced Motion. As noted above, the acoustic radiation force is responsible for the levitation of the particles, and the lateral component of acoustic radiation force drives particles toward nodes within the levitation plane.^{33,34} The streaming induced drag force tends to form vortical patterns within the fluid and contributes to the organization of spinning chains or spindles in the system.^{23,34,35} One can modulate both forces by controlling the power input.³⁶ Because the acoustic radiation force in the vertical direction is strong, when the amplitude of the actuating wave is gradually reduced to the piezoelectric transducer, it is possible to sharply diminish acoustic streaming while keeping the nanorods in the levitation plane. The disassembly of spinning chains occurs when streaming is no longer a dominant factor in the particle motion in the levitation plane. By simultaneously monitoring the speed of autonomous axial motion as well as other patterns in the chamber, one can thus gain additional insight into the forces responsible for propulsion.

Gold nanorods ($1.4 \pm 0.1 \mu\text{m}$ long) were placed in the acoustic chamber and levitated at resonance (3.77 MHz) at 10 V peak-to-peak (pp) driving amplitude. After 30 s, random autonomous motion, spinning chains and nodal aggregates were established. The amplitude of the driving voltage was then reduced by 1 Vpp every 10 s. The disassembly of spinning chains coincided with a sharp reduction in the speed of random autonomous propulsion, as shown in Figure 6. This observation provides further support that the streaming-induced drag force drives the autonomous axial motion of nanorods in regions far from the lateral nodes in the cell. The speed of axial rod movement was found to be proportional to the square of the amplitude of the driving voltage, as predicted by the streaming model (Figure 6).³⁷

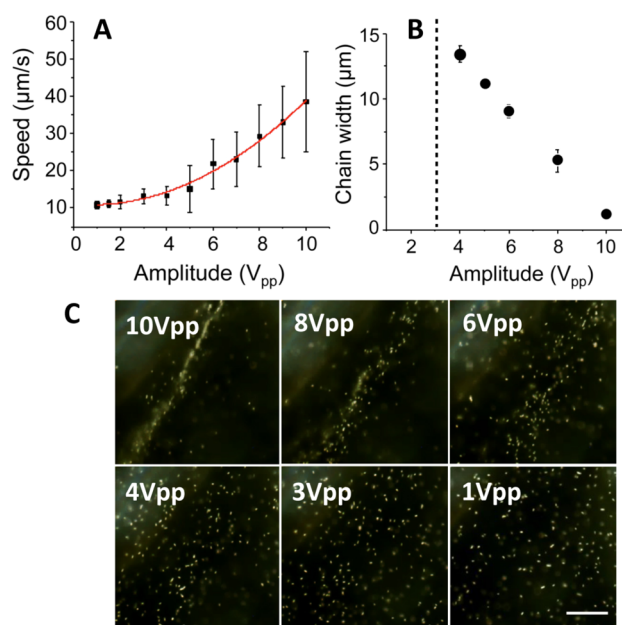


Figure 6. (A) The amplitude (voltage peak to peak) dependence of the speed of autonomous axial motion of nanorod motors. (B) The amplitude dependence of the width of a spinning chain. The dashed line marks the amplitude at which the width of the chain is greater than $40 \mu\text{m}$ field of view, which corresponds to the plateau in speed of the axially propelled rods in (A). (C) Frames showing the disbanding of a spinning chain with decreasing amplitude. Scale bar represents $10 \mu\text{m}$.

CONCLUSIONS

The movement of bimetallic nanorods was studied in order to gain insight into the shape- and material dependence of acoustic propulsion. When the densities of the two metal segments are similar, shape asymmetry determines the direction of motion, which is toward the concave end. The speed decreases with increasing length, consistent with the theory that axial motion that is driven predominantly by the streaming-induced drag force. There is also a correlation between the disassembly of spinning chains of rods and the slowing of axial autonomous motion, again consistent with streaming-induced motion. Interestingly bimetallic nanorods are consistently propelled in a polar fashion with the lower density metal segment leading. The effects of metal density on rod speeds and direction of motion are so far not explained in the streaming-induced drag force model, suggesting that some simplifying assumptions of the model may need to be re-examined.

The ability to control the direction of motion of bimetallic rods through either shape or material parameters should expand the utility of acoustic motors in sensing, diagnostics, and other potential applications. For example, catalytically powered motors have recently been shown to exhibit rheotaxis (powered movement up or downstream) as a consequence of their shape asymmetry.³⁸ Similar effects might be realized in fuel-free systems with acoustic propulsion by using bimetallic rods that are tapered at one end. Such motors could be used, for example, for targeted delivery to tumors that have high internal pressure and outward flow.

MATERIALS AND METHODS

Nanorod Fabrication and Release. Metals Au, Rh, Pd, Ag, Pt, and Ru were electrochemically deposited from commercial plating solutions within the pores of anodic alumina templates obtained from Whatman. The nominal pore diameter of the membranes was 0.2 μm , but the cross-sectional diameter through the bulk of the membrane was 300 ± 30 nm. A 350 nm layer of Ag evaporated on one side of the alumina template served as the cathode. A 350 nm evaporated Cu layer was the cathode for the AuAg sample terminated by Ag, in order to selectively dissolve the cathode layer without etching away the Ag segment of the wire. Au, Rh, Pd, Ag, and Pt were deposited using a two electrode cell under constant current conditions with a Pt coil serving as the pseudoreference/counter electrode. Au was deposited from Au-Orotemp24 RTU (Technic, Inc.) at a cathodic current of 1.24 mA/cm² with a deposition time of 13 min yielding a 1 μm segment. Rh, Pd, Ag, and Pt were deposited from Technic Rhodium RTU, Pallaspeed VHS-RTU, 1025 RTU and Platinum TP RTU (Technic, Inc.) at constant current densities of 1.76, 0.88, 2.21, and 1.76 mA/cm². Under these conditions for Rh, Pd, Ag, and Pt, deposition times of 120, 20, 8, and 40 min, respectively, yielded 1 μm segments of the metal. Ru metal was deposited at a constant potential of -0.650 V in a three-electrode cell with a Ag/AgCl reference electrode and a Pt coil counter electrode from Ru-U solution (Technic, Inc.). A 25 min deposition yielded a 1 μm segment of Ru. In all cases, a sacrificial Ag segment (Cu segment in the case of electrodeposited Ag) was plated directly onto the evaporated Ag cathode (Cu cathode in the case of Ag) prior to the deposition of the metal of interest. The length of the sacrificial segment in all cases was approximately 10 μm . Cu was deposited from a 0.1 M copper sulfate solution at a constant current density of 0.88 mA/cm² with a Pt coil counter electrode for 1 h to obtain a 10 μm sacrificial segment. Bimetallic wires were fabricated by changing the deposition solution within the cell. After deposition, the cathode material and sacrificial segment were selectively dissolved. The silver cathode and sacrificial segment were dissolved in a 1:1 water/concentrated nitric acid solution by soaking the membrane for 20 min. The copper cathode and sacrificial segment were dissolved in a proprietary copper etchant solution, Copper Etch BTP (Technic, Inc.), by soaking for 1 h. The alumina membrane was then dissolved by soaking it in 2 M aqueous NaOH overnight. Multiple rinsing steps were then done, involving repeated centrifugation, removal of the supernatant and filling the centrifuge tube with water, to suspend the wires in water.

Nanorod Characterization. FE-SEM images of nanorod samples were obtained to determine the length of the rods and the length of each metal segment. At least 21 rods were measured per sample. X-ray powder diffraction patterns of nanorod samples, still embedded in the membrane after removal of the Ag or Cu sacrificial layer, were obtained over a range of 10–90° 2 θ angles. Typically, one-fourth of the membrane, which had an area of 0.44 cm², was used in X-ray diffraction experiments. Scherrer analysis of the X-ray diffraction patterns reveal that the average grain size within the Ru metal segments is 4.3 nm, while it is 10.7 nm, more than double the value, for Rh. Hence, the packing of the Rh gains within the segment is more compact than that for Ru which may result in a slight reduction of the density of the Ru segment relative to Rh.

Acoustic Chamber. The cylindrical acoustic chamber consists of a stainless steel plate (4.2 cm \times 4.2 cm \times 1 mm), a few layers of Kapton tape (180 μm height) with a 5 mm hole punched in the center defining the chamber and a thickness mode piezoelectric transducer (1 mm thick, PZ26 Ferroperm, Kvistgard, Denmark) attached *via* epoxy (Chemtronics, ITW, Kennesaw, GA) to the other side of the stainless steel plate. The center of the cell had a resonance frequency (levitation frequency) of 3.77 MHz. An amplitude of 10 V peak to peak was used. To set up the standing wave within the chamber, a glass coverslip was used as a reflector.

Optical Imaging and Tracking. Optical imaging was done with an Olympus BX60 light microscope. Video capture was done in the range of 25–60 frames/s. Open access video tracking software Video Spot Tracker (http://cismm.cs.unc.edu/downloads/?dl_cat=3) was

used to track the movement of individual nanorods. To measure relative speeds of gold rods of 1.3 ± 0.1 , 2.3 ± 0.1 , 2.6 ± 0.1 , 3.5 ± 0.3 , 4.1 ± 0.2 , 4.3 ± 0.5 , and 5.2 ± 0.5 μm lengths, equal amounts of 1.3 μm rods and rods of a different length were mixed and added to the acoustic cell. Videos were recorded at 100 frames/s and analyzed with Matlab codes. During the analysis, we set the tracking program so that the short and long rods were tracked and their speeds recorded separately. Relative speeds were calculated and plotted because absolute speeds for a given rod length varied with position in the cell and from experiment to experiment.

ASSOCIATED CONTENT

Supporting Information

The Supporting Information is available free of charge on the ACS Publications website at DOI: 10.1021/acsnano.6b01344.

Optical microscope images and descriptions of videos of nanorod motion, FE-SEM images of rods, and methods of determining direction of motion and spinning chain width (PDF)

Video S1 AVI

Video S2 AVI

Video S3 AVI

Video S4 AVI

AUTHOR INFORMATION

Corresponding Author

*E-mail: tem5@psu.edu.

Notes

The authors declare no competing financial interest.

ACKNOWLEDGMENTS

We thank Julie Anderson for assistance with FE-SEM imaging, and François Nadal and Eric Lauga for helpful discussions. This work was supported by the National Science Foundation under MRSEC Grant DMR-1420620. Analytical instrumentation used in this work was supported by the Pennsylvania State University Materials Research Institute Nanofabrication Laboratory under National Science Foundation Cooperative Agreement ECS-0335765. W.W. is grateful for the financial support from National Natural Science Foundation of China (Grant No. 11402069) and Shenzhen Peacock Technological Innovation Program (Grant No. KQCX20140521144102503).

REFERENCES

- (1) Wang, W.; Duan, W.; Ahmed, S.; Mallouk, T. E.; Sen, A. Small Power: Autonomous Nano- and Micromotors Propelled by Self-Generated Gradients. *Nano Today* **2013**, *8*, 531–534.
- (2) Mallouk, T.; Sen, A. Powering Nanorobots. *Sci. Am.* **2009**, *300*, 72–77.
- (3) Gibbs, J. G.; Fischer, P. Active colloidal microdrills. *Chem. Commun.* **2015**, *51*, 4192–4195.
- (4) Roche, J.; Carrara, S.; Sanchez, J.; Lannelongue, J.; Loget, G.; Bouffier, L.; Fischer, P.; Kuhn, A. Wireless Powering of e-Swimmers. *Sci. Rep.* **2014**, *4*, 6705.
- (5) Guix, M.; Mayorga-Martinez, C. C.; Merkoçi, A. Nano/Micromotors in (Bio)chemical Science Applications. *Chem. Rev.* **2014**, *114*, 6285–6322.
- (6) Peyer, K. E.; Tottori, S.; Qiu, F.; Zhang, L.; Nelson, B. J. Magnetic Helical Micromachines. *Chem. - Eur. J.* **2013**, *19*, 28–38.
- (7) Wang, H.; Pumera, M. Fabrication of Micro/Nanoscale Motors. *Chem. Rev.* **2015**, *115*, 8704–8735.
- (8) Sanchez, S.; Soler, L.; Katuri, J. Chemically Powered Micro- and Nanomotors. *Angew. Chem., Int. Ed.* **2015**, *54*, 1414–1444.

- (9) Yadav, V.; Pavlick, R. A.; Meckler, S. M.; Sen, A. Triggered Detection and Deposition: Toward the Repair of Microcracks. *Chem. Mater.* **2014**, *26*, 4647–4652.
- (10) Kar, A.; Chiang, T.; Rivera, I. O.; Sen, A.; Velegol, D. Enhanced Transport into and out of Dead-End Pores. *ACS Nano* **2015**, *9*, 746–753.
- (11) Wang, W.; Castro, L. A.; Hoyos, M.; Mallouk, T. E. Autonomous Motion of Metallic Microrods Propelled by Ultrasound. *ACS Nano* **2012**, *6*, 6122–6132.
- (12) Ahmed, S.; Wang, W.; Mair, L. O.; Fraleigh, R. D.; Li, S.; Castro, L. A.; Hoyos, M.; Huang, T. J.; Mallouk, T. E. Steering Acoustically Propelled Nanowire Motors toward Cells in a Biologically Compatible Environment Using Magnetic Fields. *Langmuir* **2013**, *29*, 16113–16118.
- (13) Wang, W.; Li, S.; Mair, L.; Ahmed, S.; Huang, T. J.; Mallouk, T. E. Acoustic Propulsion of Nanorod Motors inside Living Cells. *Angew. Chem., Int. Ed.* **2014**, *53*, 3201–3204.
- (14) Garcia-Gradilla, V.; Sattayasamitsathit, S.; Soto, F.; Kuralay, F.; Yardimci, C.; Wiitala, D.; Galarnyk, M.; Wang, J. Ultrasound-Propelled Nanoporous Gold Wire for Efficient Drug Loading and Release. *Small* **2014**, *10*, 4154–4159.
- (15) Esteban-Fernández de Ávila, B.; Martín, A.; Soto, F.; Lopez-Ramirez, M. A.; Campuzano, S.; Vásquez-Machado, G. M.; Gao, W.; Zhang, L.; Wang, J. Single Cell Real-Time miRNAs Sensing Based on Nanomotors. *ACS Nano* **2015**, *9*, 6756–6764.
- (16) Li, J.; Li, T.; Xu, T.; Kiristi, M.; Liu, W.; Wu, Z.; Wang, J. Magneto–Acoustic Hybrid Nanomotor. *Nano Lett.* **2015**, *15*, 4814–4821.
- (17) Rao, K. J.; Li, F.; Meng, L.; Zheng, H.; Cai, F.; Wang, W. A Force to Be Reckoned With: A Review of Synthetic Microswimmers Powered by Ultrasound. *Small* **2015**, *11*, 2836–2846.
- (18) Ahmed, S.; Gentekos, D. T.; Fink, C. A.; Mallouk, T. E.; Al, A. E. T. Self-Assembly of Nanorod Motors into Geometrically Regular Multimers and Their Propulsion by Ultrasound. *ACS Nano* **2014**, *8*, 11053–11060.
- (19) Wang, W.; Duan, W.; Zhang, Z.; Sun, M.; Sen, A.; Mallouk, T. E. A Tale of Two Forces: Simultaneous Chemical and Acoustic Propulsion of Bimetallic Micromotors. *Chem. Commun.* **2015**, *51*, 1020–1023.
- (20) Xu, T.; Soto, F.; Gao, W.; Dong, R.; Garcia-Gradilla, V.; Magaña, E.; Zhang, X.; Wang, J. Reversible Swarming and Separation of Self-Propelled Chemically Powered Nanomotors under Acoustic Fields. *J. Am. Chem. Soc.* **2015**, *137*, 2163–2166.
- (21) Garcia-Gradilla, V.; Orozco, J.; Sattayasamitsathit, S.; Soto, F.; Kuralay, F.; Pourazary, A.; Katzenberg, A.; Gao, W.; Shen, Y.; Wang, J. Functionalized Ultrasound-Propelled Magnetically Guided Nanomotors: Toward Practical Biomedical Applications. *ACS Nano* **2013**, *7*, 9232–9240.
- (22) Nadal, F.; Lauga, E. Asymmetric Steady Streaming as a Mechanism for Acoustic Propulsion of Rigid Bodies. *Phys. Fluids* **2014**, *26*, 082001.
- (23) Castro, A.; Hoyos, M. Study of the Onset of the Acoustic Streaming in Parallel Plate Resonators with Pulse Ultrasound. *Ultrasonics* **2016**, *66*, 166–171.
- (24) Wiklund, M.; Green, R.; Ohlin, M. Acoustofluidics 14: Applications of Acoustic Streaming in Microfluidic Devices. *Lab Chip* **2012**, *12*, 2438–2451.
- (25) Wang, Y.; Hernandez, R. M.; Bartlett, D. J.; Bingham, J. M.; Kline, T. R.; Sen, A.; Mallouk, T. E. Bipolar Electrochemical Mechanism for the Propulsion of Catalytic Nanomotors in Hydrogen Peroxide Solutions. *Langmuir* **2006**, *22*, 10451–10456.
- (26) Raeymaekers, B.; Pantea, C.; Sinha, D. N. Manipulation of Diamond Nanoparticles Using Bulk Acoustic Waves. *J. Appl. Phys.* **2011**, *109*, 014317.
- (27) Bruus, H. Acoustofluidics 7: The Acoustic Radiation Force on Small Particles. *Lab Chip* **2012**, *12*, 1014–1021.
- (28) *CRC Handbook of Chemistry and Physics*, 96th ed.; Haynes, W. M., Ed.; CRC Press, 2015; pp 12–206.
- (29) Seymour, R. J.; O'Farrelly, J. Platinum-Group Metals. *Kirk-Othmer Encyclopedia of Chemical Technology*; John Wiley & Sons, Inc., 2001; p 6.
- (30) *CRC Handbook of Chemistry and Physics*, 96th ed.; Hayes, W. M., Ed.; CRC Press, 2015; pp 14–46.
- (31) Muller, P. B.; Barnkob, R.; Jensen, M. J. H.; Bruus, H. A Numerical Study of Microparticle Acoustophoresis Driven by Acoustic Radiation Forces and Streaming-Induced Drag Forces. *Lab Chip* **2012**, *12*, 4617–4627.
- (32) Barnkob, R.; Augustsson, P.; Laurell, T.; Bruus, H. Acoustic Radiation- and Streaming-Induced Microparticle Velocities Determined by Microparticle Image Velocimetry in an Ultrasound Symmetry Plane. *Phys. Rev. E - Stat. Nonlinear, Soft Matter Phys.* **2012**, *86*, 056307.
- (33) Evander, M.; Nilsson, J. Acoustofluidics 20: Applications in Acoustic Trapping. *Lab Chip* **2012**, *12*, 4667–4676.
- (34) Woodside, S. M.; Bowen, B. D.; Piret, J. M. Measurement of Ultrasonic Forces for Particle–liquid Separations. *AIChE J.* **1997**, *43*, 1727–1736.
- (35) Aktas, M. K.; Farouk, B. Numerical Simulation of Acoustic Streaming Generated by Finite-Amplitude Resonant Oscillations in an Enclosure. *J. Acoust. Soc. Am.* **2004**, *116*, 2822–2831.
- (36) Hoyos, M.; Castro, A. Controlling the Acoustic Streaming by Pulsed Ultrasounds. *Ultrasonics* **2013**, *53*, 70–76.
- (37) Bruus, H. *Theoretical Microfluidics*; Oxford University Press, 2008.
- (38) Palacci, J.; Sacanna, S.; Abramian, A.; Barral, J.; Hanson, K.; Grosberg, A. Y.; Pine, D. J.; Chaikin, P. M. Artificial Rheotaxis. *Sci. Adv.* **2015**, *1*, e1400214.